

316L 不锈钢双激光选区熔化成形性能研究

樊胜杰, 杨永强, 宋长辉*, 刘子彬

华南理工大学机械与汽车工程学院, 广东 广州 510641

摘要 为了研究不同的扫描模式对激光选区熔化(SLM)成形质量的影响,采用自主研发的双激光同步扫描激光选区熔化设备,在单激光扫描、双激光低功率同步扫描、双激光高速同步扫描模式下制备了 316L 不锈钢样件,对比了三种模式下的成形质量,分析了三种模式下飞溅形态、熔池形貌以及样件力学性能的差异。结果表明:采用双激光低功率(110 W)同步扫描时,由反冲压力引起的飞溅增多,熔池尺寸均匀且排列整齐;随着单束激光功率从 95 W 提升至 120 W,样件的致密度从 98.91% 提升至 99.32%;样件的微观组织主要由宽度为 0.65~0.75 μm 的柱状亚晶与等轴亚晶组成。采用双激光高速(2000 mm/s)同步扫描时,熔池深宽发生较大变化,搭接率由单激光扫描时的 30% 提升至 50% 以上,柱状亚晶的平均尺寸由单激光扫描时的 0.50 μm 降到 0.35 μm 。两种双激光同步扫描模式下成形样件的力学性能与单激光扫描模式下的相当,致密度达到 99% 以上,抗拉强度均超过 720 MPa,延伸率超过 40%。双激光高速同步扫描使得成形效率相较单激光扫描提升了一倍,为大尺寸激光选区熔化设备的扫描策略设计提供了新思路。

关键词 激光技术; 金属增材制造; 激光选区熔化; 316L 不锈钢; 双激光; 能量密度; 力学性能

中图分类号 TG665

文献标志码 A

DOI: 10.3788/CJL221233

1 引言

激光选区熔化(SLM)被认为是最具前景的增材技术之一^[1]。它采用高能量密度激光作为热源,金属粉末在激光照射下熔化并凝固成形。目前激光选区熔化方面的研究多集中于钛合金^[2-3]、铝合金^[4-5]、镍基合金^[6-7]、铜合金^[8-9]、铁基合金^[10-11]、不锈钢等材料,其中,316L 奥氏体不锈钢具有优异的可成形性,是研究最早也是研究最多的材料之一。此外,316L 不锈钢中含有较高含量(质量分数为 16%~18%)的 Cr 元素,其表面可形成富 Cr 的致密氧化膜,使基体钝化,从而具有优异的耐蚀性和抗氧化能力^[12]。因此,316L 不锈钢在石油化工、医疗、机械制造等领域^[13]都有非常广泛的应用。

Jiang 等^[14]研究了激光功率和能量密度对缺陷的影响,结果显示:在相同的能量密度下,高激光功率成形的零件比低激光功率成形的零件具有更高的致密度;随着能量密度增大,缺陷的数量先减少后增加。Wang 等^[15]发现,在 316L 凝固过程中,由于温度梯度和热流方向不同,熔池不同区域的结晶类型不同:在熔池底部,晶粒先以平面生长的方式向外延伸,然后以胞状枝晶的方式发育;在熔池中部,仅存在胞状枝晶;在熔池顶部,胞状枝晶沿激光扫描方向向最大热流方向转

变。Liu 等^[16]研究发现,在激光功率不变的情况下,高扫描速度下成形的样品中可以观察到具有高比例小角度晶界的细小晶粒以及具有纳米夹杂物的蜂窝状结构,该样品的抗拉强度可以达到 707 MPa,断裂伸长率为 30%。解妙霞等^[17]在基板预热的条件下成形了 316L 不锈钢,结果发现预热对力学性能的影响不显著。

经过众多学者的研究,316L 不锈钢的激光选区熔化成形工艺已经较为成熟,近几年的研究热点是如何在保证成形质量的同时提高成形效率。提高激光扫描速率或增加成形激光束数量是两种常见提高成形效率的方法^[18-20]。已有学者的研究表明,单激光成形时,采用高功率、高扫描速度的策略会导致成形件的力学性能和成形质量下降^[21]。此外,采用高激光功率成形容易对光学器件造成损伤,如 Jadhav 等^[22]在利用激光选区熔化工序打印纯铜时,由于激光能量过高,再加上纯铜对红外激光的反射率高,光学系统出现了损伤。能否通过双光束同步的方式在不增加单一振镜负荷的情况下提高熔池的热输入呢?

本文提出了一种双光束同步扫描方法,并在相同的能量密度输入条件下采用单激光、双激光低功率同步扫描(两束激光的功率降为单激光扫描模式下的一半,其余参数不变)以及双激光高速同步扫描(两束激光的扫描速度是单激光扫描模式下的两倍,其余参数

收稿日期: 2022-09-13; 修回日期: 2022-10-19; 录用日期: 2022-11-22; 网络首发日期: 2022-12-04

基金项目: 国家自然科学基金(U2001218)、广东省重点领域研发计划(2020B090923001)

通信作者: *chsong@scut.edu.cn

不变)对 316L 不锈钢进行了激光选区熔化成形实验,探讨了三种模式对成形质量的影响,对比并分析了上述三种成形模式下 316L 不锈钢微观组织和力学性能的差异,为多振镜多激光选区熔化设备的高效成形研究提供实验支持与理论依据。

2 实验材料及方法

2.1 实验设备

使用自主研发的 Dimetal 280 双激光选区熔化系

统进行实验,该系统搭载两台功率为 500 W 的光纤激光器,激光器输出激光的波长为 1070~1090 nm;采用 3D 高速扫描振镜,该振镜通过可以移动的镜片实现动态聚焦,其原理如图 1 所示。双激光选区熔化设备的最大成形尺寸为 250 mm×250 mm×300 mm。打印过程中使用氮气作为保护气体。在开始打印工作之前,先向成形舱内充入氮气,使成形舱内氧气的体积分数控制在 1.0×10^{-5} 以下,以便进行后续的打印工作。

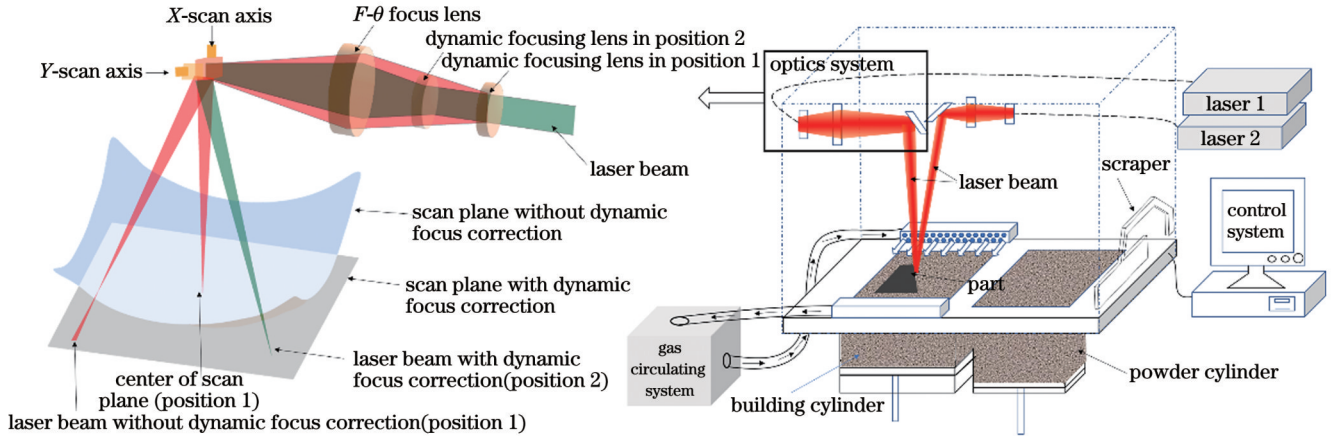


图 1 成形系统的工作原理

Fig. 1 Working principle of forming system

2.2 实验材料

实验材料是采用气雾化制粉工艺制备的 316L 不锈钢粉末,图 2(a)是 316L 不锈钢粉末的扫描电镜

(SEM)照片及化学成分;图 2(b)是粒径分布图。由图 2 可知,粉末具有较好的球形度,其粒径范围为 29~54 μm ,粒径中值为 39 μm 。

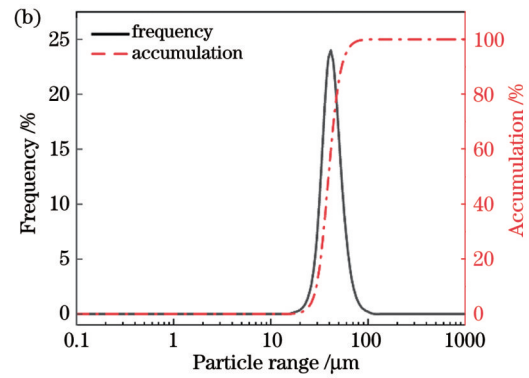
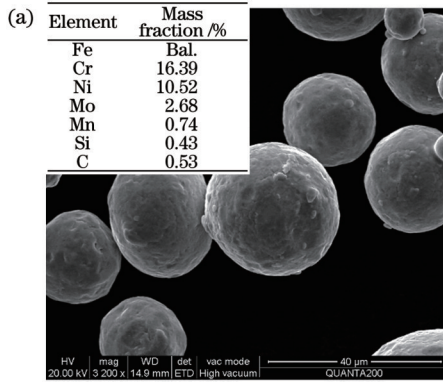


图 2 316L 不锈钢粉末的形貌、成分及粒径分布。(a)SEM 形貌及化学成分;(b)粒径分布

Fig. 2 Morphology, chemical composition, and particle size distribution of 316L stainless steel powder. (a) SEM morphology and chemical composition; (b) particle range

2.3 实验方法

2.3.1 成形工艺参数

在前期的单激光成形实验探究中得到了最佳的工艺参数,即:激光功率 $P=220 \text{ W}$,扫描速度 $v=1000 \text{ mm/s}$,铺粉层厚 $t=30 \mu\text{m}$,扫描间距 $h=70 \mu\text{m}$ 。在此基础上,本文探究不同能量输入模式对零件成形质量的影响。使用双激光同步扫描进行打印时,按照输入能量密度不变的原则进行初步的实验设计。在成形过程

中,激光的体能量密度 ω 的计算公式为

$$\omega = \frac{P}{h \times v \times t}, \quad (1)$$

式中: P 为激光功率, W; h 为扫描间距, μm ; v 为扫描速度, mm/s ; t 为铺粉厚度, μm 。依据本实验中单激光的最优参数可以计算得到能量密度为 $\omega=104.76 \text{ J/mm}^3$ 。在进行双激光低功率同步扫描时,每束激光的功率是单激光功率的一半(为 110 W),其余参数不变;在进行

双激光高速同步扫描时,速度为单激光扫描下的两倍(为 2000 mm/s),其余参数不变。为了更好地研究参数变化

对性能的影响,适当调整了工艺参数的范围,所采用的 316L 不锈钢激光选区熔化成形工艺参数如表 1 所示。

表 1 316L 不锈钢粉末激光选区熔化成形工艺参数
Table 1 Selective laser melting (SLM) process parameters of 316L stainless steel

Energy input mode	No.	Power /W	Scanning speed / (mm·s ⁻¹)	Energy density / (J·mm ⁻³)
Single laser	1	200	1000	95.2381
	2	210	1000	100.0000
	3	220	1000	104.7619
	4	230	1000	109.5238
	5	240	1000	114.2857
Dual-laser low-power	6	100×2	1000	95.2381
	7	105×2	1000	100.0000
	8	110×2	1000	104.7619
	9	115×2	1000	109.5238
	10	120×2	1000	114.2857
Dual-laser high-speed	11	200×2	2000	95.2381
	12	210×2	2000	100.0000
	13	220×2	2000	104.7619
	14	230×2	2000	109.5238
	15	240×2	2000	114.2857

2.3.2 实验样品以及扫描策略

制备 10 mm×10 mm×10 mm 的立方体试样进行微观组织分析。为了准确观测熔池的形貌特征,将扫描角度设为 0°,如图 3(a)所示。拉伸件的尺寸较大,而

较长的扫描线可能会引起较大的内应力^[23],从而影响拉伸性能。为了降低成形过程中残余应力的影响,拉伸件成形采用的扫描方式是 45°倾斜层间正交旋转扫描^[24],如图 3(b)所示。

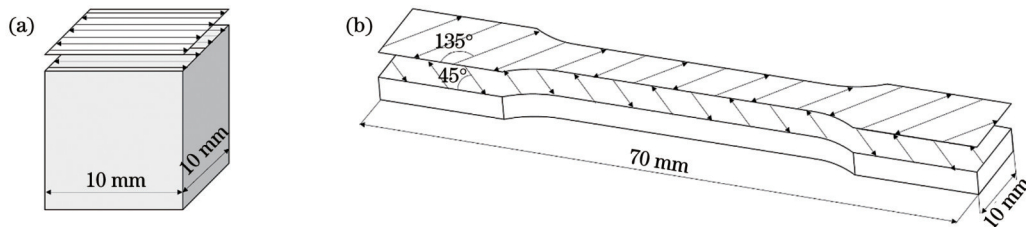


图 3 样件尺寸示意图。(a)立方体试样;(b)拉伸件
Fig. 3 Schematics of sample size. (a) Cube sample; (b) tensile sample

2.4 测试方法

2.4.1 飞溅观察

采用高速摄影机对成形过程中的飞溅进行拍摄,拍摄角度约为 45°,水平距离约为 200 mm,曝光时间为 500 μs,帧率为 1288 frame/s,放大倍数为 0.97。高速摄影机与激光选区熔化成形设备的位置关系如图 4 所示。

2.4.2 致密度测试

为了尽可能保证数据的准确性,在相同的参数下打印两个试样,每个试样分别进行 3 次测量,求其平均值。试样的致密度采用阿基米德排水法测定,具体的

计算公式为

$$\rho = \frac{m_{\text{air}} \times \rho_{\text{H}_2\text{O}}}{\rho_0 \times (m_{\text{air}} - m_{\text{H}_2\text{O}})}, \quad (2)$$

式中: $\rho_0=7.98 \text{ g/cm}^3$, 是 316L 不锈钢的理论密度; $\rho_{\text{H}_2\text{O}}=1.00 \text{ g/cm}^3$, 是水的密度; $m_{\text{H}_2\text{O}}$ 表示样品在水中的质量; m_{air} 表示样品在空气中的质量。

2.4.3 力学性能测试

采用 CMT5105 万能试验机进行拉伸性能测试,测试在大气室温环境下进行,拉伸速度为 1 mm/min。

2.4.4 微观组织表征

对金相表征试样进行打磨、抛光,然后采用稀释的

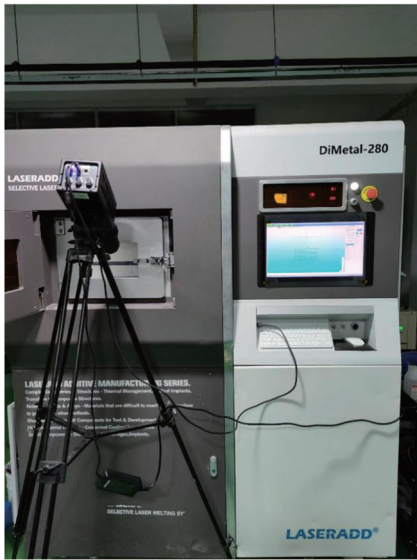


图4 激光选区熔化设备与高速摄影机的位置关系

Fig. 4 Position relationship between SLM equipment and high-speed camera

王水(由 HNO_3 、 HCl 、 H_2O 按体积比为 1:3:6 配制而成)进行腐蚀,腐蚀时间为 60~90 s。采用金相显微镜和 NovaTMNanoSEM 430 扫描电子显微镜对激光选区熔化成形试样的熔池形貌和微观组织进行观测。

3 实验结果及分析

3.1 工艺参数对飞溅的影响

在激光选区熔化成形过程中,高能激光束使熔池上方产生反冲压力,低的反冲压力有利于熔池变平,而过高的反冲压力会使熔融材料飞离熔池形成飞溅^[25-26]。同时,温度过高导致的金属急剧蒸发与气相膨胀会带动熔池周围的粉末飞出,形成另一种飞溅^[27-28]。Wang 等^[29]将 CoCr 合金激光选区熔化过程中的飞溅分为金属射流、熔滴飞溅和粉末飞溅三种,如图 5 所示。飞溅会影响铺粉质量以及激光照射在粉末上的均匀性,导致样件内部产生欠熔颗粒、气孔或残渣等缺陷,进而影响样件的力学性能。

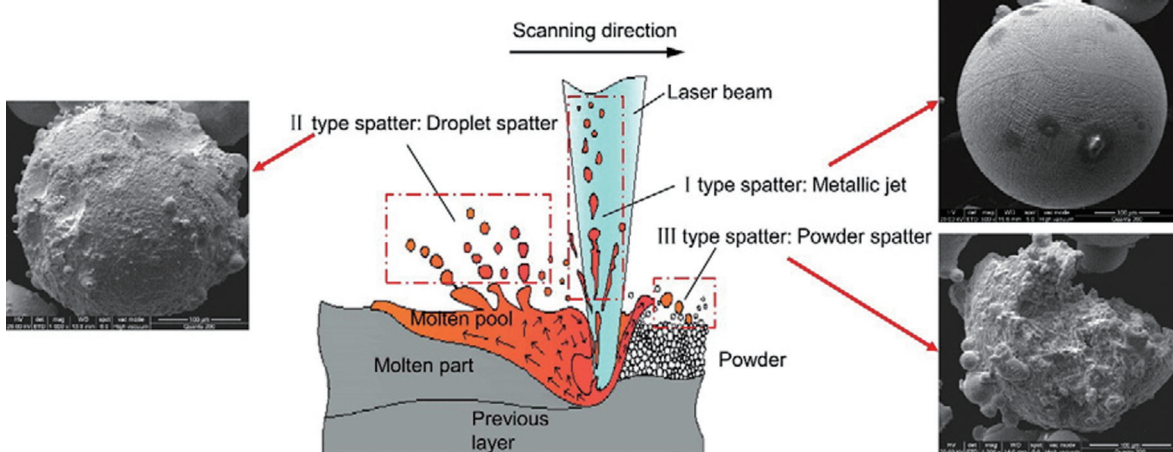


图5 三种不同类型的飞溅^[29]

Fig. 5 Three different types of splashes^[29]

通过高速相机捕获的飞溅的形态如图 6 所示。成形过程中,熔融金属液体表面在汽化压力与重力的作用下瞬间坍塌,与气相膨胀产生的反冲力碰撞产生熔滴飞溅。相比于单激光,双激光低功率同步扫描时的金属射流飞溅增加,熔滴飞溅大幅减少。这是因为双光束的叠加有利于熔池在深度方向的增加(见 3.3 节),相邻熔池底部的高度差变大,使得更多气体发生膨胀,产生更大的反冲压力,导致金属射流增多,如图 7(a)所示。

双激光高速同步扫描时,激光与粉末相互作用的时间随扫描速度的提升而减少。激光束能量的增加以及激光与粉末相互作用时间的缩短必然会引起更高的温度梯度,加剧了马兰戈尼效应,熔融的金属液体以更高的速度从熔池的高温底部流向后部的低温侧壁和边缘^[30-31],部分液体以一定的初速度飞离熔池,形成熔滴飞溅,如图 7(b)所示。由于极高的扫描速度,飞溅的

速度相比单激光、双激光低功率同步扫描成形方式下的更快。

3.2 工艺参数对致密度的影响

样件的致密度测试结果如图 8 所示。在单激光模式下,当功率低于 220 W 时,样件的致密度随着功率的提升而提升;当激光功率超过 220 W 时,致密度随着功率的提升而下降,这是因为过高的功率使得粉末过度烧蚀形成了不规则孔隙^[32]。除此之外,过高的功率也容易导致熔池的反冲压力增强,产生更多飞溅,从而导致气孔等缺陷的产生^[33]。

在双激光低功率同步扫描情况下,当激光功率较低(100 W)时,样件的致密度低于 99%。进一步提升激光功率,使能量密度与单激光成形模式下的相当时,两种成形模式下样件的致密度相近。随着能量密度进一步增加,样件的致密度略高于单激光成形样件的致密度。由此可知,与单激光相比,双激光低功率成形样

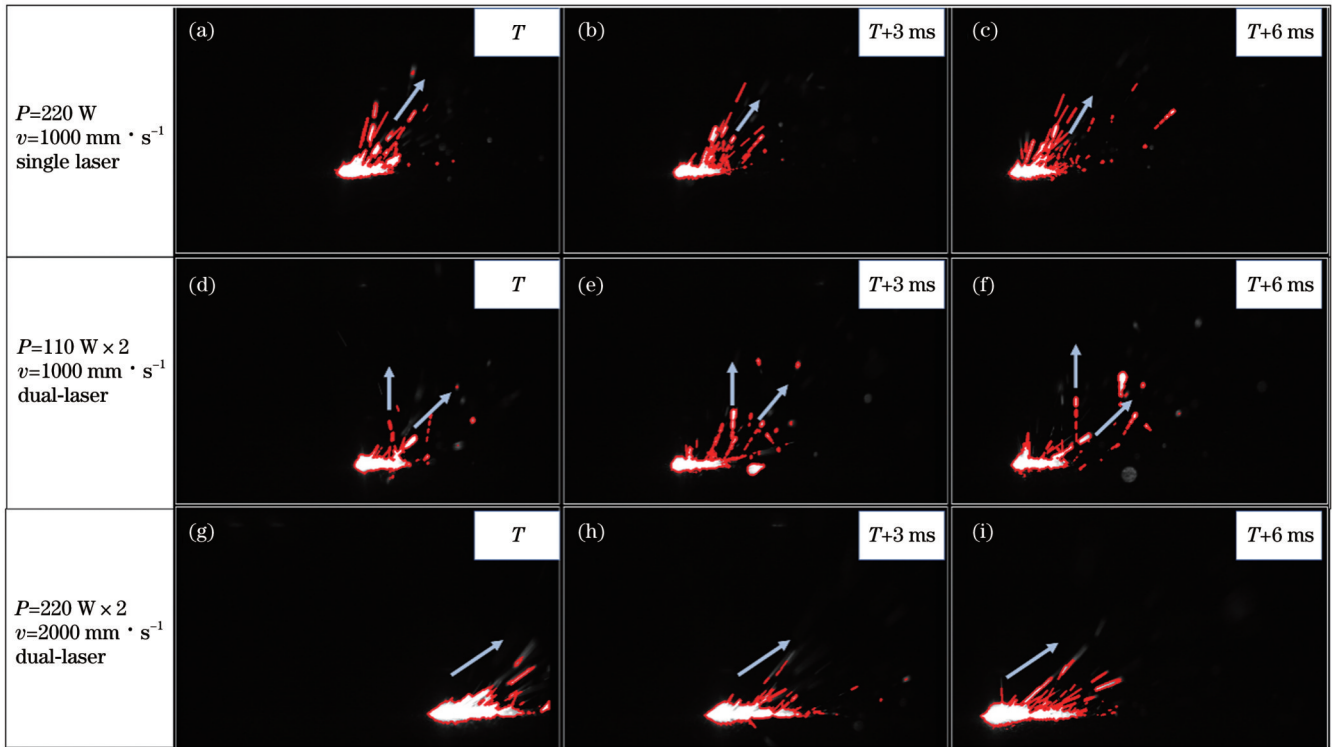


图 6 高速相机捕获的飞溅动态图。(a)~(c)单激光扫描;(d)~(f)双激光低功率同步扫描;(g)~(i)双激光高速同步扫描

Fig. 6 Dynamic variation images of spatters captured by high speed camera. (a)–(c) Single laser scanning; (d)–(f) dual-laser low-power synchronous scanning; (g)–(i) dual-laser high-speed synchronous scanning

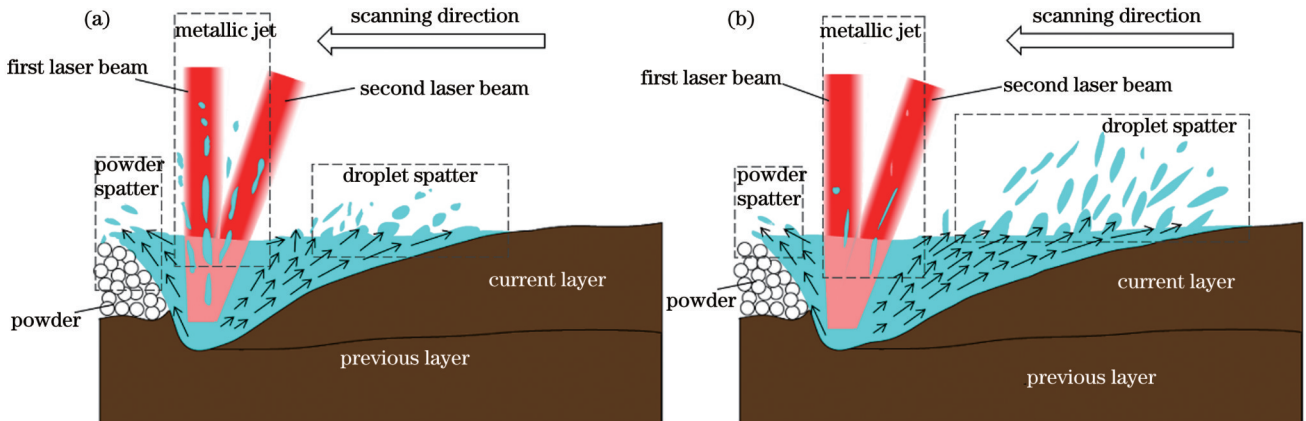


图 7 飞溅的形成机制。(a)双激光低功率同步扫描;(b)双激光高速同步扫描

Fig. 7 Forming mechanism of spatters. (a) Dual-laser low-power synchronous scanning; (b) dual-laser high-speed synchronous scanning

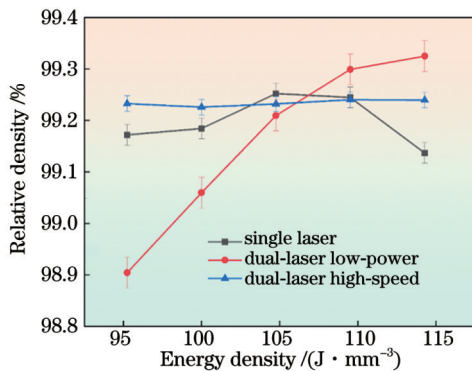


图 8 能量密度对致密度的影响

Fig. 8 Effect of energy density on relative density

件的致密度对激光功率更为敏感,并随着功率的增大而线性增大。这是因为在双激光低功率同步扫描情况下,当激光功率较低时,熔池温度相对较低,熔池的流动性较差,熔池内滞留的气体无法及时逸出,导致熔池内部产生了气孔缺陷,降低了样件的致密度。

在双激光高速同步扫描情况下,样件的致密度与单激光情况下的相当,如图 8 所示,而且致密度的变化范围极小。其原因可能是在激光功率较低时,双激光高速同步扫描也能达到成形所需的能量阈值。

由此可以看出,能量密度公式存在一定局限性,其对于单激光扫描可取得较好的效果,但对于多激光成

形,还需要进一步分析多束激光相互作用的机理。体积能量密度作为一个热力学量,无法描述过程中发生的物理现象(马兰戈尼流、反冲压力、流体力学不稳定性等)^[34]。这些较难定性考量的物理现象会显著影响样件的成形过程,只借助能量密度公式无法体现其影响,从而降低了其适用性。

本次实验发现,在双激光高速同步扫描下,随着激光功率变化,样件致密度的波动幅度小于单激光成形样件,说明该模式下可能存在更大的工艺窗口。这与 Kamath 等^[35]研究 316L 不锈钢时得到的结论相同,即:采用高激光功率成形时,扫描速度允许选择的窗口范围更大。

3.3 工艺参数对微观组织的影响

相比于单激光模式,双激光低功率同步扫描模式

下的熔池更为均匀,相邻熔池底部的高度差从 $32 \mu\text{m} \pm 5 \mu\text{m}$ 增加到 $40 \mu\text{m} \pm 5 \mu\text{m}$,约增加了 25%,如图 9 所示。由于激光光斑呈高斯分布,当激光功率降低时,能达到粉末熔点的圆形区域减小,但两激光束是同步扫描,第二束光斑的大部分能量直接作用于熔池而非粉末,因此熔池深度有所增加。由图 9 还可以看出,当功率较低时,熔池内部产生了更多孔洞。de Terris 等^[36]研究了能量密度对激光选区熔化 316L 构件气孔率的影响,结果发现低能量密度下粉末熔化不充分,样件中出现了非球形孔洞。考虑到熔池形状连续且均匀,并且大多数孔洞位于非边界区域,说明该类孔洞并不是由能量不足导致的,很可能是熔池内部流动性和润湿性较差,导致一些气体来不及逸出而产生了孔洞。

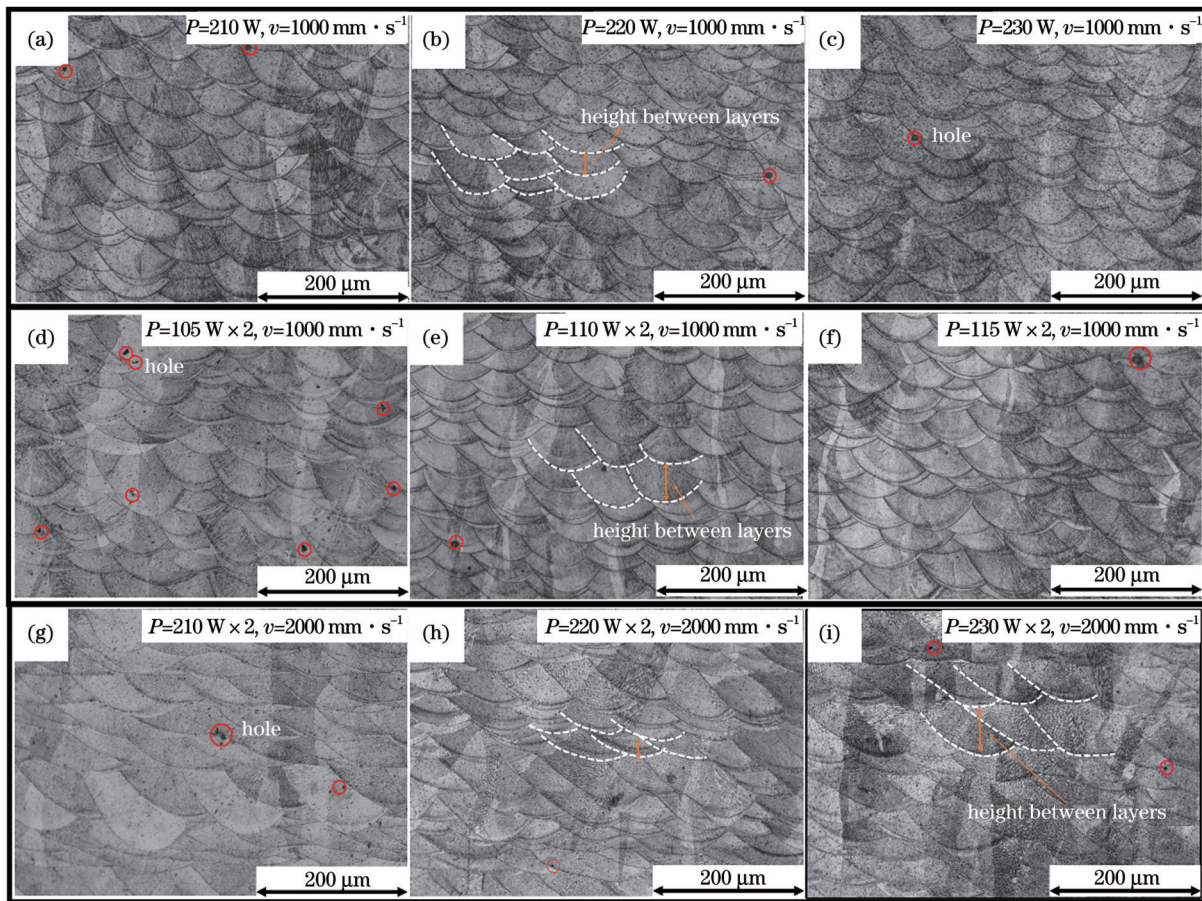


图 9 不同工艺参数下样件的熔池形貌。(a)~(c)单激光扫描;(d)~(f)双激光低功率同步扫描;(g)~(i)双激光高速同步扫描
Fig. 9 Molten pool morphologies of samples under different process parameters. (a)~(c) Single laser scanning; (d)~(f) dual-laser low-power synchronous scanning; (g)~(i) dual-laser high-speed synchronous scanning

在双激光高速同步扫描模式下,随着激光功率改变,熔池存在浅且宽与深且宽两种形态,如图 9(h)、(i)所示。与单激光扫描形成的熔池相比,双激光高速同步扫描下形成的熔池首先是宽度方向发生了明显变化,宽度方向的搭接率超过了 50%。Bertoli 等^[34]通过研究发现:随着体积能量密度增大,熔池宽度和熔池深度均增大。激光束与粉末接触时,热量沿着水平、垂

直两个方向传播,由于光斑大小以及激光能量呈高斯分布的限制,熔池的宽度并不会随激光功率的升高而一直增大,多余的能量会向深度方向扩散,增加熔池的深度。在双激光高速同步成形模式下,当功率较低时,易产生宽而浅的熔池;当功率增加至 240 W 时,能量过高,导致当前层与上一层熔池结合,形成了一个更大的熔池。

在成形过程中,熔池上方是激光束与气体,下方是凝固层,热量向下传递的速度更快,而晶粒总是朝着散热最快的方向生长^[37],所以在图 10 展示的熔池的 SEM 图像中,晶粒内部的亚晶结构都朝着熔池边界线的法线方向。对于熔池两侧边缘来说,由于晶粒生

长方向的差异性,必然会在中间形成晶界,这种现象在不同的成形模式下均有体现。此外,激光会对上一层进行重熔,因此可以看到柱状亚晶由于热传递而出现了跨越多层熔池的外延生长现象,如图 10(a) 所示。

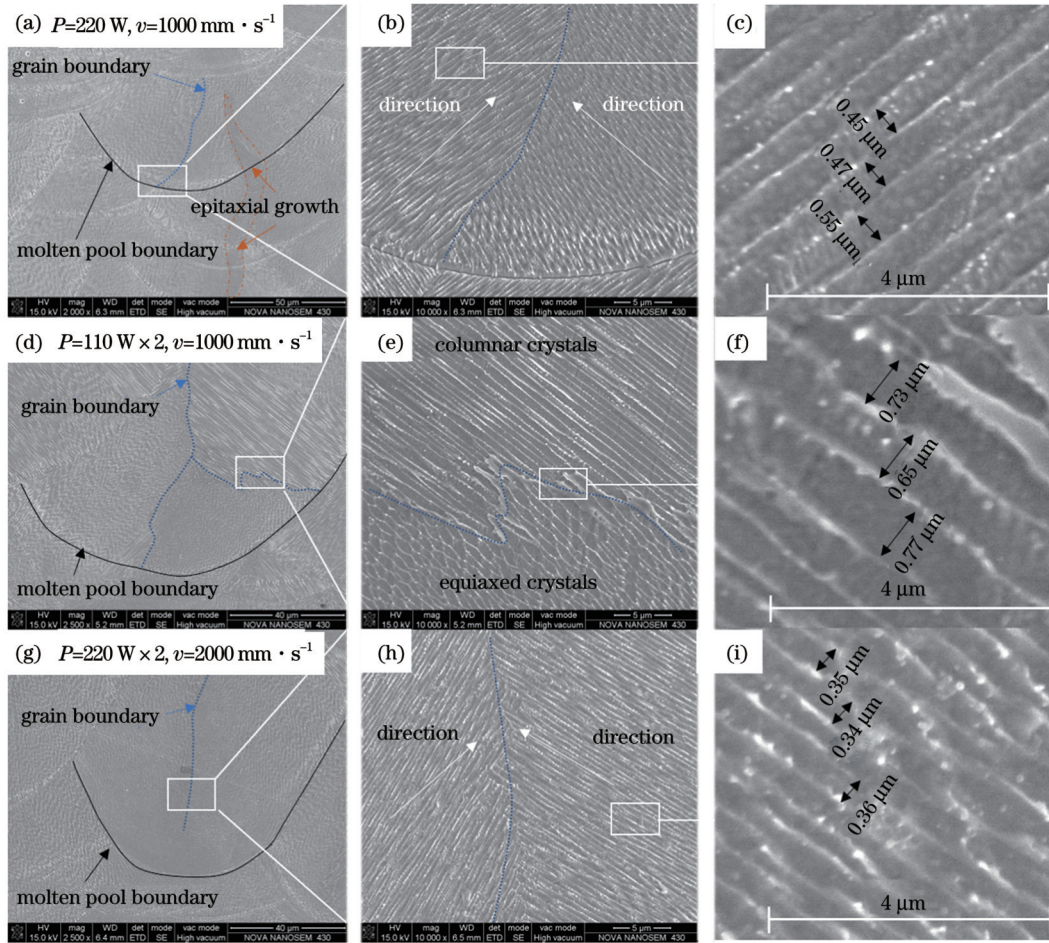


图 10 316L 成形样件的 SEM 图。(a)~(c) 单激光扫描;(d)~(f) 双激光低功率同步扫描;(g)~(i) 双激光高速同步扫描
Fig. 10 SEM images of 316L forming samples. (a)~(c) Single laser; (d)~(f) dual-laser low-power synchronous scanning; (g)~(i) dual-laser high-speed synchronous scanning

熔池具有极快的凝固速率和较大的温度梯度,因此晶粒内形成了尺寸更小的柱状亚晶与胞状亚晶。合金凝固组织的形态受 G/R 和 $G \times R$ 的综合影响,其中: G 是温度梯度,单位为 K/m ; R 是凝固速率,单位为 m/s 。 G/R 决定着凝固模式, G/R 值的降低促使晶粒由柱状到等轴状转变; $G \times R$ 决定着凝固组织的尺寸, $G \times R$ 值的增大有利于细化凝固组织^[38]。在单激光扫描下,单个熔池内部的晶粒以宽度为 $0.45 \sim 0.55 \mu m$ 的柱状亚晶为主,如图 10(c) 所示。在双激光低功率同步扫描下,熔池内部出现了等轴亚晶、被拉长的等轴亚晶以及柱状亚晶的混合晶粒,晶粒的宽度均在 $0.65 \sim 0.75 \mu m$ 之间,拉长的等轴亚晶的长度从 $0.60 \mu m$ 到 $30 \mu m$ 不等,并逐渐过渡为柱状亚晶,如图 10(f) 所示。扫描速度不变,随着激光能量降低, G/R 减小,有助于等轴晶出现,同时, $G \times R$ 的值也相

应减小,所得到的柱状枝晶的平均尺寸略有增大。在双激光高速同步扫描下,双倍激光能量的输入以及扫描速度的提升使得凝固速率与温度梯度都有所增加, $G \times R$ 的值增大,因此相比于单激光成形样件,其柱状亚晶尺寸变小,平均尺寸从单激光成形试样的 $0.50 \mu m$ 降到 $0.35 \mu m$,如图 10(i) 所示。

3.4 工艺参数对力学性能的影响

激光选区熔化制备的样件内部具有多层次、多尺度的微观结构特征,分别包括激光扫描产生的熔池、粒内胞晶偏析网络结构(简称“细胞结构”)和原位形成的氧化物纳米夹杂物^[14]。这些多层次的微观结构被认为是同时提高激光选区熔化成形 316L 不锈钢零件强度和延展性的主要因素之一^[39-40]。选取三组致密度最佳样件的成形参数进行拉伸样件的制备,并测试拉伸样件的力学性能,具体测试结果如表 2 所示。

表 2 316L 不锈钢样件的拉伸测试结果
Table 2 Tensile test results of 316L stainless steel samples

Process parameter	Tensile strength /MPa	Yield strength /MPa	Strain /%
$P=220\text{ W}, v=1000\text{ mm}\cdot\text{s}^{-1}$	732.18 ± 15	594.30 ± 15	44.12 ± 2
$P=120\text{ W}\times 2, v=1000\text{ mm}\cdot\text{s}^{-1}$	731.90 ± 15	584.58 ± 15	44.07 ± 2
$P=220\text{ W}\times 2, v=2000\text{ mm}\cdot\text{s}^{-1}$	739.73 ± 15	603.47 ± 15	42.58 ± 2

从表 2 所示数据可以看出,三种扫描模式下样件的力学性能基本持平,抗拉强度大于 720 MPa,延伸率

超过 40%。不同扫描模式下样件的应力-应变曲线如图 11(a)所示,强度及应变的均值如图 11(b)所示。

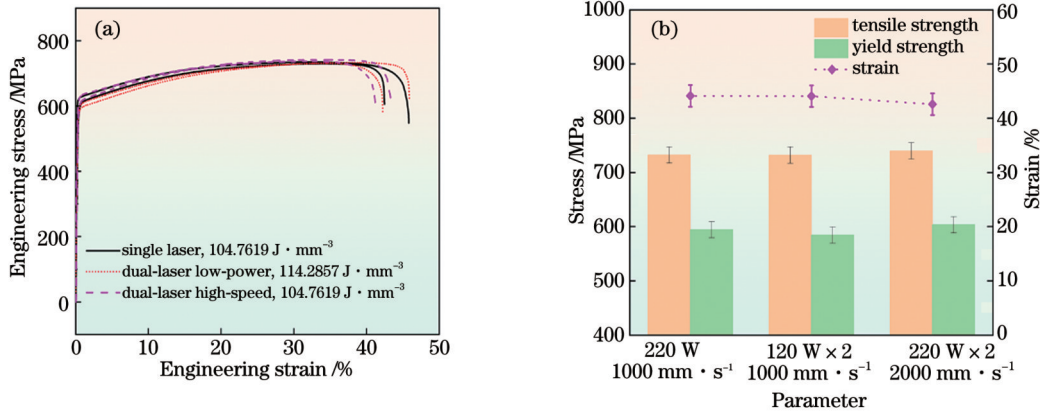


图 11 不同扫描模式下样件的力学性能。(a)应力-应变曲线;(b)均值直方图

Fig. 11 Mechanical properties of samples formed in different laser scanning modes. (a) Stress-strain curves; (b) mean value histogram

316L 不锈钢拉伸件的断口形貌如图 12 所示。韧窝是塑性变形过程中材料内部的微小孔洞经形核、扩展、合并最后相互连接形成的。三种扫描模式下的拉伸断口上都可以明显地观察到大量韧窝,并且大部分韧窝的尺寸都是亚微米级与纳米级,这表明三者都属于韧性断裂。晶粒细化有利于提升力学性能。上文提到,在双激光同步扫描下,柱状枝晶的宽度减小,但力学性能相差并不大。可能的原因之一是在三种扫描模式下,样件的力学性能已经达到极限水平,通过双激光扫描的方式很难进一步提升其力学性能。

4 结 论

将双激光低功率同步扫描和双激光高速同步扫描作为实验组,以单激光扫描作为对照组,进行了不同扫描方式下成形的可行性探究,研究了不同扫描方式下飞溅形态、熔池形貌以及样件微观组织和力学性能的差异。得到的主要结论有:

1) 两种双激光同步扫描方式均可成形 316L 不锈钢样件,样件的致密度均在 99% 以上,抗拉强度均能达到 720 MPa,延伸率均超过了 40%。

2) 在单激光扫描与双激光高速同步扫描下,晶粒均以柱状亚晶为主,双激光高速同步扫描模式下的亚晶宽度为 $0.35\ \mu\text{m}$,小于单激光扫描模式下的亚晶宽度 ($0.50\ \mu\text{m}$)。双激光低功率同步扫描下的样件中同时存在柱状亚晶、等轴亚晶以及被拉长的等轴亚晶,晶粒宽度在 $0.65\sim 0.75\ \mu\text{m}$ 之间。

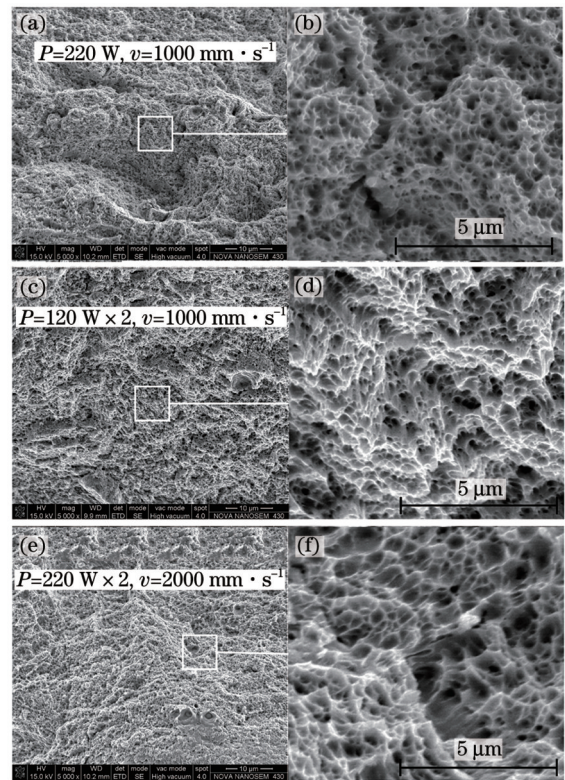


图 12 拉伸样件的断口形貌。(a)~(b)单激光扫描;(c)~(d)双激光低功率同步扫描;(e)~(f)双激光高速同步扫描

Fig. 12 Fracture morphologies of tensile samples. (a)–(b) Single laser scanning; (c)–(d) dual-laser low-power synchronous scanning; (e)–(f) dual-laser high-speed synchronous scanning

3) 与单激光扫描相比,双激光高速同步扫描方式能够将成形效率提升一倍。

参 考 文 献

- [1] He W, Shi W, Li J, et al. *In-situ* monitoring and deformation characterization by optical techniques; part I: laser-aided direct metal deposition for additive manufacturing[J]. Optics and Lasers in Engineering, 2019, 122: 74-88.
- [2] 单奇博, 刘忱, 姚静, 等. 扫描策略对激光熔化沉积态 TC4 钛合金组织性能及残余应力的影响[J]. 激光与光电子学进展, 2021, 58(11): 1114002.
Shan Q B, Liu C, Yao J, et al. Effects of scanning strategy on the microstructure, properties, and residual stress of TC4 titanium alloy prepared by laser melting deposition[J]. Laser & Optoelectronics Progress, 2021, 58(11): 1114002.
- [3] Galarraga H, Lados D A, Dehoff R R, et al. Effects of the microstructure and porosity on properties of Ti-6Al-4V ELI alloy fabricated by electron beam melting (EBM) [J]. Additive Manufacturing, 2016, 10: 47-57.
- [4] Siddique S, Imran M, Wycisk E, et al. Influence of process-induced microstructure and imperfections on mechanical properties of AlSi12 processed by selective laser melting[J]. Journal of Materials Processing Technology, 2015, 221: 205-213.
- [5] Tang M, Pistorius P C. Oxides, porosity and fatigue performance of AlSi10Mg parts produced by selective laser melting[J]. International Journal of Fatigue, 2017, 94: 192-201.
- [6] LeBrun T, Nakamoto T, Horikawa K, et al. Effect of retained austenite on subsequent thermal processing and resultant mechanical properties of selective laser melted 17-4 PH stainless steel[J]. Materials & Design, 2015, 81: 44-53.
- [7] Rafi H K, Pal D, Patil N, et al. Microstructure and mechanical behavior of 17-4 precipitation hardenable steel processed by selective laser melting[J]. Journal of Materials Engineering and Performance, 2014, 23(12): 4421-4428.
- [8] Zhou Y, Zeng X, Yang Z, et al. Effect of crystallographic textures on thermal anisotropy of selective laser melted Cu-2.4Ni-0.7Si alloy [J]. Journal of Alloys and Compounds, 2018, 743: 258-261.
- [9] Sabelle M, Walczak M, Ramos-Grez J. Scanning pattern angle effect on the resulting properties of selective laser sintered monolayers of Cu-Sn-Ni powder[J]. Optics and Lasers in Engineering, 2018, 100: 1-8.
- [10] Sun Z J, Tan X P, Tor S B, et al. Simultaneously enhanced strength and ductility for 3D-printed stainless steel 316L by selective laser melting[J]. NPG Asia Materials, 2018, 10(4): 127-136.
- [11] Ji L, Lu J P, Liu C M, et al. Microstructure and mechanical properties of 304L steel fabricated by arc additive manufacturing[J]. MATEC Web of Conferences, 2017, 128: 03006.
- [12] 余晨帆, 赵聪聪, 张哲峰, 等. 选区激光熔化 316L 不锈钢的拉伸性能[J]. 金属学报, 2020, 56(5): 683-692.
Yu C F, Zhao C C, Zhang Z F, et al. Tensile properties of selective laser melted 316L stainless steel[J]. Acta Metallurgica Sinica, 2020, 56(5): 683-692.
- [13] 顾冬冬, 张红梅, 陈洪宇, 等. 航空航天高性能金属材料构件激光增材制造[J]. 中国激光, 2020, 47(5): 0500002.
Gu D D, Zhang H M, Chen H Y, et al. Laser additive manufacturing of high-performance metallic aerospace components [J]. Chinese Journal of Lasers, 2020, 47(5): 0500002.
- [14] Jiang H Z, Li Z Y, Feng T, et al. Effect of process parameters on defects, melt pool shape, microstructure, and tensile behavior of 316L stainless steel produced by selective laser melting[J]. Acta Metallurgica Sinica (English Letters), 2021, 34(4): 495-510.
- [15] Wang D, Song C, Yang Y, et al. Investigation of crystal growth mechanism during selective laser melting and mechanical property characterization of 316L stainless steel parts[J]. Materials & Design, 2016, 100: 291-299.
- [16] Liu J W, Song Y, Chen C, et al. Effect of scanning speed on the microstructure and mechanical behavior of 316L stainless steel fabricated by selective laser melting[J]. Materials & Design, 2020, 186: 108355.
- [17] 解妙霞, 辛琪珂, 李焱鑫, 等. 预热对选区激光熔化 316L 不锈钢力学性能的影响[J]. 中国激光, 2022, 49(8): 0802016.
Xie M X, Xin Q K, Li Y X, et al. Effect of preheating on mechanical properties of 316L stainless steel fabricated by selective laser melting[J]. Chinese Journal of Lasers, 2022, 49(8): 0802016.
- [18] Zhang C C, Zhu H, Hu Z, et al. A comparative study on single-laser and multi-laser selective laser melting AlSi10Mg: defects, microstructure and mechanical properties[J]. Materials Science and Engineering: A, 2019, 746: 416-423.
- [19] Li F Z, Wang Z, Zeng X. Microstructures and mechanical properties of Ti6Al4V alloy fabricated by multi-laser beam selective laser melting[J]. Materials Letters, 2017, 199: 79-83.
- [20] Masoomi M, Thompson S M, Shamsaei N. Quality part production via multi-laser additive manufacturing[J]. Manufacturing Letters, 2017, 13: 15-20.
- [21] 宗学文, 高倩, 周宏志, 等. 体激光能量密度对选区激光熔化 316L 不锈钢各向异性的影响[J]. 中国激光, 2019, 46(5): 0502003.
Zong X W, Gao Q, Zhou H Z, et al. Effects of bulk laser energy density on anisotropy of selective laser sintered 316L stainless steel [J]. Chinese Journal of Lasers, 2019, 46(5): 0502003.
- [22] Jadhav S D, Dadbakhsh S, Goossens L, et al. Influence of selective laser melting process parameters on texture evolution in pure copper[J]. Journal of Materials Processing Technology, 2019, 270: 47-58.
- [23] Zou S, Xiao H, Ye F, et al. Numerical analysis of the effect of the scan strategy on the residual stress in the multi-laser selective laser melting[J]. Results in Physics, 2020, 16: 103005.
- [24] Cheng B, Shrestha S, Chou K. Stress and deformation evaluations of scanning strategy effect in selective laser melting[J]. Additive Manufacturing, 2016, 12: 240-251.
- [25] Fabbro R, Hamadou M, Coste F. Metallic vapor ejection effect on melt pool dynamics in deep penetration laser welding[J]. Journal of Laser Applications, 2004, 16(1): 16-19.
- [26] Fabbro R, Slimani S, Doudet I, et al. Experimental study of the dynamical coupling between the induced vapour plume and the melt pool for Nd-YAG CW laser welding[J]. Journal of Physics D: Applied Physics, 2006, 39(2): 394-400.
- [27] Qiu C L, Panwisawas C, Ward M, et al. On the role of melt flow into the surface structure and porosity development during selective laser melting[J]. Acta Materialia, 2015, 96: 72-79.
- [28] Andani M T, Dehghani R, Karamooz-Ravari M R, et al. Spatter formation in selective laser melting process using multi-laser technology[J]. Materials & Design, 2017, 131: 460-469.
- [29] Wang D, Wu S, Fu F, et al. Mechanisms and characteristics of spatter generation in SLM processing and its effect on the properties[J]. Materials & Design, 2017, 117: 121-130.
- [30] 范思远, 毛家智, 谢颂伟, 等. 脉冲/连续双光束复合激光熔覆对 316L 不锈钢熔覆组织的影响[J]. 中国激光, 2023, 50(4): 0402008.
Fan S Y, Mao J Z, Xie S W, et al. Effect of pulsed/continuous double beam hybrid laser cladding on the microstructure of 316L stainless steel[J]. Chinese Journal of Lasers, 2023, 50(4): 0402008.
- [31] Dai D H, Gu D. Tailoring surface quality through mass and momentum transfer modeling using a volume of fluid method in selective laser melting of TiC/AlSi10Mg powder[J]. International Journal of Machine Tools and Manufacture, 2015, 88: 95-107.
- [32] 徐凯池, 王科, 徐如雪, 等. 激光选区熔化成型 316L 不锈钢工艺参数研究[J]. 航空发动机, 2022, 48(1): 110-115.
Xu K C, Wang K, Xu R X, et al. Study on process parameters of selective laser melting 316L stainless steel[J]. Aeroengine, 2022, 48(1): 110-115.

- [33] 刘畅, 马行驰, 马海彬. 工艺参数对 SLM 成型 316L 不锈钢致密度的影响及缺陷表现方式[J]. 热加工工艺, 2021, 50(12): 44-49.
Liu C, Ma X C, Ma H B. Effect of process parameters on density of 316L stainless steel by SLM and defects manifestation methods [J]. Hot Working Technology, 2021, 50(12): 44-49.
- [34] Bertoli U S, Wolfer A J, Matthews M J, et al. On the limitations of volumetric energy density as a design parameter for selective laser melting[J]. Materials & Design, 2017, 113: 331-340.
- [35] Kamath C, El-Dasher B, Gallegos G F, et al. Density of additively-manufactured, 316L SS parts using laser powder-bed fusion at powers up to 400 W[J]. The International Journal of Advanced Manufacturing Technology, 2014, 74(1): 65-78.
- [36] de Terris T, Andreau O, Peyre P, et al. Optimization and comparison of porosity rate measurement methods of selective laser melted metallic parts[J]. Additive Manufacturing, 2019, 28: 802-813.
- [37] Gong H J, Rafi K, Gu H, et al. Analysis of defect generation in Ti-6Al-4V parts made using powder bed fusion additive manufacturing processes[J]. Additive Manufacturing, 2014, 1/2/3/4: 87-98.
- [38] Sahn P R, Jones H, Adam C M. Science and technology of the undercooled melt: rapid solidification materials and technologies [M]. Dordrecht: Springer Netherlands, 1986.
- [39] Wang Y M, Kamath C, Voisin T, et al. A processing diagram for high-density Ti-6Al-4V by selective laser melting[J]. Rapid Prototyping Journal, 2018, 24(9): 1469-1478.
- [40] Zhong Y, Liu L, Wikman S, et al. Intragranular cellular segregation network structure strengthening 316L stainless steel prepared by selective laser melting[J]. Journal of Nuclear Materials, 2016, 470: 170-178.

Properties of 316L Stainless Steel Formed by Dual-Laser Selective Melting

Fan Shengjie, Yang Yongqiang, Song Changhui*, Liu Zibin

School of Mechanical & Automotive Engineering, South China University of Technology, Guangzhou 510641, Guangdong, China

Abstract

Objective In order to explore the differences of selective laser melting (SLM) formation in three modes: single laser scanning, dual-laser low-power synchronous scanning (the power of two lasers becomes half of the power of the single laser, and the other parameters remain unchanged) and dual-laser high-speed synchronous scanning (the speed of two lasers becomes double of the speed of the single laser, and the other parameters remain unchanged), we investigated the feasibility of forming stainless steel with the dual-laser and the impact of the techniques on forming quality. The study provides experimental support and a theoretical basis for high-efficiency forming research of multi-galvanometer multi-laser selective melting equipment.

Methods Self-developed dual-laser synchronous scanning equipment was used to form 316L stainless steel samples under the same energy density through single-laser and dual-laser synchronous scanning. The corrosion samples were used to observe the morphology and microstructure of the molten pool. Finally, according to the above results, appropriate process parameters were selected, tensile samples were prepared, the mechanical properties of the samples formed with three modes were compared, and the fracture morphology was observed.

Results and Discussions As far as spatter is concerned, compared with a single laser, dual-laser low-power synchronous scanning method is beneficial for increasing the depth of the molten pool and increases the metallic jet. At the same time, in dual-laser high-speed synchronous scanning mode, owing to the increase in the laser beam energy and shortened interaction time between the laser and powder, a higher temperature gradient occurs, which aggravates the Marangoni effect. The high-temperature bottom of the molten pool flows to the low-temperature sidewalls and rear edges, and more liquid flows from the molten pool at a certain initial velocity, thereby increasing the droplet spatter (Fig. 6).

Compared with the single laser forming sampler, the density of dual-laser low-power synchronous scanning formed sample is more sensitive to the laser power and increases linearly with the increase in power. This is owing to the influence of the superposition of the double beams. When the laser power is low, the temperature of the molten pool is relatively low, resulting in poor fluidity, and the retained gas cannot escape the molten pool in time, resulting in internal pore defects, which reduces the relative density of the sample. For dual-laser high-speed synchronous scanning, the density of the sample is comparable to that of a single laser and the range of density variation is extremely small. This may be because the energy threshold required for shaping is achieved even at relatively low laser power.

Compared with the single laser mode, the molten pool distribution of dual-laser low-power synchronous scanning was more uniform, and the distance between the bottoms of the molten pools increases by approximately 25%, from $32 \mu\text{m} \pm 5 \mu\text{m}$ to $40 \mu\text{m} \pm 5 \mu\text{m}$ (Fig. 9). Because the laser spot has a Gaussian distribution, when the laser power is reduced, the circular area that can reach the melting point decreases, but the two laser beams are scanned synchronously, and most of the energy of the second beam spot acts directly on the molten pool instead of the powder; hence, the depth of the molten pool increases. However, for dual-laser high-speed synchronous scanning, with the increase of laser power, the molten pool becomes wide and deep from wide and shallow. Compared to the molten pool formed by a single laser, the width direction changed significantly, and the most intuitive change is that the overlap ratio exceeds 50%. The laser beam is in contact with the powder, and heat spreads in the horizontal and vertical directions. For dual-

laser high-speed synchronous scanning forming in this experiment, when the power is low, it is easy to produce a wide and shallow molten pool. When the power is increased to 240 W, an excessively high power causes the current layer to combine with the molten pool of the previous layer, resulting in a larger molten pool.

Conclusions 1) The dual-laser synchronous scanning method can be used to form 316L stainless steel samples. The density of the samples is above 99%, the tensile strength can reach 720 MPa, and the elongation rate exceeds 40%, meeting application requirements.

2) Both single laser forming and dual-laser high-speed synchronous scanning forming, the interior of the grain is dominated by columnar subcrystals, but the width of the single laser subcrystal is 0.50 μm , while the latter is approximately 0.35 μm . Columnar, equiaxed, and elongated equiaxed subcrystals coexist under dual-laser low-power synchronous scanning mode.

3) Dual-laser high-speed synchronous scanning method can double the forming efficiency.

Key words laser technique; metal additive manufacturing; selective laser melting; 316L stainless steel; dual-laser; energy density; mechanical properties